Optics Communications 402 (2017) 662–667

Contents lists available at ScienceDirect

Optics Communications

journal homepage: www.elsevier.com/locate/optcom

Laser-based dual-space microscopy

Maged Alotaibi [a,b,*], Robert Gedies [a], Abdullah Alzayed [a], Fahad Aldawsari [a], Daniel Dominguez [a,b], Luis Grave de Peralta [a,b]

[a] Department of Physics, Texas Tech University, Lubbock, TX 79409, USA
[b] Nano Tech Center, Texas Tech University, Lubbock, TX 79409, USA

ARTICLE INFO

Keywords:
Microscopy
Imaging systems
Phase recovery

ABSTRACT

We show using two-dimensional simulations that the dual-space microscopy (DSM) phase-recovery algorithm converges to the correct result for arbitrary samples. We present experimental results obtained by implementing the DSM technique using a laser. We demonstrate that DSM produces synthetic images with a large field of view when a laser is used as the illumination source. However, speckles affect the quality of the obtained images.

1. Introduction

Fourier ptychographic microscopy (FPM) is a phase-recovery imaging technique [1–9] that permits to obtain high-resolution images with a large field of view (FOV) from a set of low-resolution images obtained by illuminating the sample from a different direction each time [10–15]. FPM was initially demonstrated using planar [10–12] and hemispherical [13,14] arrays of light emitting diodes (LED) as white-light illumination sources and it was subsequently extended to the infrared spectral range [16]. FPM was also demonstrated using a laser as the illumination source, and mirrors to illuminate the sample from different directions using the same laser beam [16–18]. The low-resolution images of the sample used in FPM only record the intensity of the electric field in the microscope's real plane (RP). Nevertheless, in general, the FPM phase-recovery algorithm is successful in extracting the unmeasured phase of the electric field in the sample's plane because each low-resolution RP image carries partial information about the phase. The resolution limit of FPM is $\sim \lambda/NA_s$, where λ is the wavelength of the light used for imaging, $NA_s = NA_o + NA_c$, and NA_o and NA_c are the numerical apertures of the objective lens and condenser, respectively [12,14,15]. Therefore, when $NA_c > NA_o$, FPM permits to obtain images with better resolution than the Rayleigh resolution limit $\sim \lambda/(2NA_o)$ [10]. DSM is another recently demonstrated phase-recovery imaging technique which is based on the simultaneous observation of the sample in the position and momentum spaces; i.e., the DSM phase-recovery algorithm can be considered an extension of the FPM algorithm where intensity images obtained in the microscope's Fourier plane (FP) are used in addition to the low-resolution RP images used in FPM [18,19]. When DSM was demonstrated using a hemispherical array of LEDs, it was found that the obtained high-resolution RP images have a reduced FOV due to the small divergence of the light emitted from each LED [18]. The solution of this problem is the main focus of this work. Here we demonstrate for the first time that synthetic images with a large FOV are obtained by implementing the DSM technique using a laser beam as the illumination source. In order to facilitate the comparison between the FPM and DSM techniques based on both laser and LEDs, we present results obtained with both phase-recovery techniques using a hemispherical digital condenser (HDC) [14,18], and using a hemispherical laser guider (HLG) fabricated with similar geometry than the HDC. The rest of this paper is organized in the following manner: In Section 2 we describe the experimental arrangements used in this work. In Section 3, the DSM algorithm is discussed and simulations results are presented. For the first time, we demonstrate using realistic two-dimensional simulations that the DSM phase-recovery algorithm works well for arbitrary samples. Experimental results are presented and discussed in Section 4. Finally, the conclusions of this work are presented in Section 5.

2. Experimental set up

We imaged a 600 lines/mm Ronchi Ruling (p = 1.67 μm) using a Nikon Elipse Ti inverted microscope with an objective lens with NA_o = 0.8 and 50X magnification. As sketched in Fig. 1(a), the microscope set up includes two charge coupled device (CCD) cameras for obtaining RP and FP images of the sample.

The microscope's built in illumination source was substituted either by a computer controlled HDC formed by 64 white-light LEDs

* Corresponding author at: Texas Tech University, Physics Department, Lubbock, TX 79409, USA.
E-mail address: maged.alotaibi@ttu.edu (M. Alotaibi).

http://dx.doi.org/10.1016/j.optcom.2017.06.085
Received 6 May 2017; Received in revised form 10 June 2017; Accepted 25 June 2017
0030-4018/

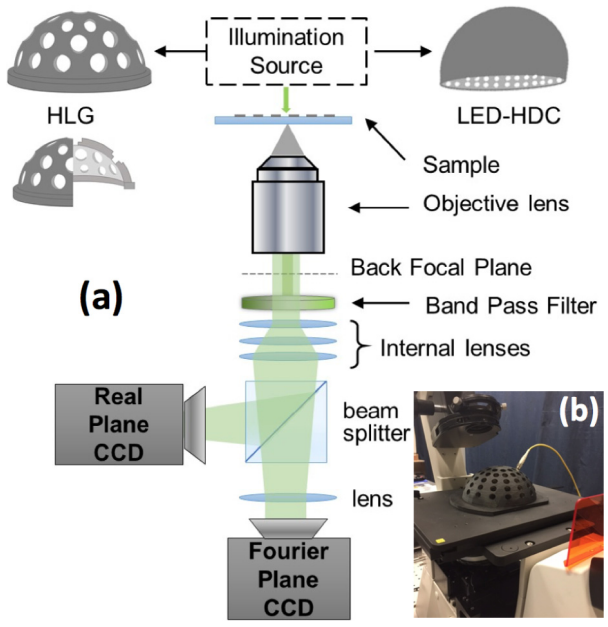

Fig. 1. (a) Schematic illustration of the experimental set up. The illumination source can be either a HDC (top-right) or a laser-HLG combination (top-left). (b) Photograph of the HLG-collimator combination.

distributed uniformly in four circular-rows having numerical apertures $NA_c = 0.58, 0.73, 0.89, 0.97$ [14,18], or by a HLG, which was fabricated by a 3D-printer with geometry similar to the HDC. As shown in Fig. 1(b), the HLG has 76 circular-holes for manually inserting a collimator connected by a single mode optical fiber to a $\lambda = 532$ nm wavelength laser beam produced by a solid-state laser. Sixty four of the 76 HLG holes permit to illuminate the sample in the same directions as the LEDs in the HDC can illuminate the sample. This allows a direct comparison of the images obtained using LED and laser illumination. Eleven of the other 12 holes in the HLG are distributed uniformly in a circular row with $NA_c = 0.37$. The last hole is located directly at the center and permits to illuminate the sample perpendicularly ($NA_c = 0$) with the laser beam. As sketched in Fig. 1(a), the HDC and the HLG were alternatively placed directly on top of the sample. When the HDC was used, a band-pass spectral filter centered at $\lambda = 570$ nm with a 10 nm bandwidth was inserted after the objective lens.

3. Dual-space microscopy

The DSM algorithm has been described in detail before [18,19]; nonetheless, here we include a fast description of it for consistency. As sketched in block (1) in Fig. 2, the DSM algorithm starts by assuming an initial approximation of the complex function describing the high-resolution optical disturbance (OD) at the microscope's RP [20]. For instance, the DSM algorithm could start by assuming that both the amplitude $\left(a_{m=0}\left(\vec{r}\right)\right)$ and the phase $\left(p_{m=0}\left(\vec{r}\right)\right)$ of the OD are equal to zero.

As shown in block (2) of Fig. 2, the input approximation is then Fourier-transformed to obtain the actual approximation of the OD in the microscope's FP:

$$A_{m,j}^{act}\left(\vec{k}\right) e^{iP_{m,j}^{act}\left(\vec{k}\right)} = F\left[a_{m=0}\left(\vec{r}\right) e^{ip_{m=0}\left(\vec{r}\right)}\right]. \tag{1}$$

As shown in block (3) in Fig. 2, Eq. (2) is used to calculate the first approximation to the amplitude $\left(A_{m,j}\left(\vec{k}\right)\right)$ and phase $\left(P_{m,j}\left(\vec{k}\right)\right)$ corresponding to the intensity $\left(A_{m,j}^2\left(\vec{k}\right)\right)$ of the FP image with small NA_o that would be observed by illuminating the sample from the direction j .

$$A_{m,j}\left(\vec{k}\right) e^{iP_{m,j}\left(\vec{k}\right)} = A_{m,j}^{act}\left(\vec{k}-\overrightarrow{k_j}\right) e^{iP_{m,j}^{act}\left(\vec{k}-\overrightarrow{k_j}\right)} \cdot W_o. \tag{2}$$

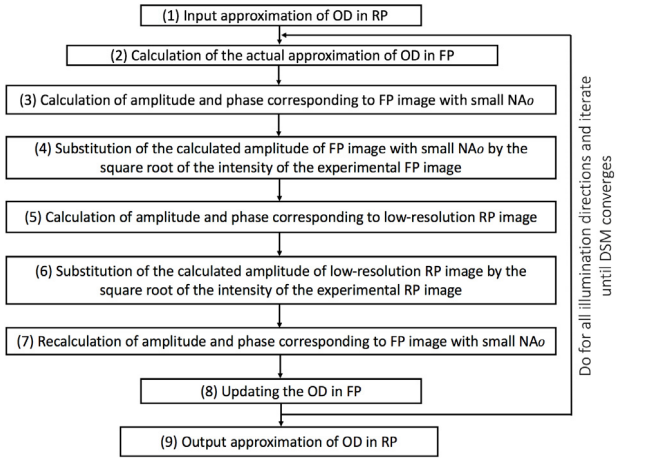

Fig. 2. Block diagram of DSM algorithm.

In Eq. (2), the magnitude of the wavevector $\overrightarrow{k_j}$ is $k_j = (2\pi/\lambda)NA_c$, where NA_c takes the value corresponding to the illumination direction j, and W_o is a circular window with radius NA_o, amplitude equal to one, and is centered at $\overrightarrow{k_j} = 0$. The step indicated in the block (4) in Fig. 2 is absent in FPM, were only RP images are used. In DSM the calculated amplitude of the FP image with small NA_o $\left(A_{m,j}\left(\vec{k}\right)\right)$ is substituted by the square root of the measured intensity of the corresponding experimental FP image with small NA_o $\left(A_j\left(\vec{k}\right)\right)$. The rest of the steps of the DSM algorithm coincide with the well-known steps of the FPM algorithm [10–15]. In short, as indicated in block (5) in Fig. 2, an inverse Fourier transform (F^{-1}) operation is performed to calculate the amplitude and phase associated with the low-resolution RP image using Eq. (3):

$$a_{m,j}\left(\vec{r}\right) e^{ip_{m,j}\left(\vec{r}\right)} = F^{-1}\left[A_j\left(\vec{k}\right) e^{iP_{m,j}\left(\vec{k}\right)}\right]. \tag{3}$$

As sketched in block (6) in Fig. 2, in the next algorithm step the calculated amplitude of the low-resolution RP image $\left(a_{m,j}\left(\vec{r}\right)\right)$ is substituted by the square root of the measured intensity of the corresponding experimental low-resolution RP image $\left(a_j\left(\vec{r}\right)\right)$ and, as shown in block (7) in Fig. 2, Eq. (4) is used to recalculate the amplitude and phase corresponding to the FP image with small NA_o:

$$A_{m,j}^{rec}\left(\vec{k}\right) e^{iP_{m,j}^{rec}\left(\vec{k}\right)} = F\left[a_j\left(\vec{r}\right) e^{ip_{m,j}\left(\vec{r}\right)}\right] \cdot W_o. \tag{4}$$

Then, as indicated in block (8) in Fig. 2, the updated approximation of the optical disturbance in the FP is calculated using Eq. (5):

$$A_{m,j}^{upd}\left(\vec{k}\right) e^{iP_{m,j}^{upd}\left(\vec{k}\right)} = A_{m,j}^{act}\left(\vec{k}\right) e^{iP_{m,j}^{act}\left(\vec{k}\right)} + \alpha\left[\gamma A_{m,j}^{rec}\left(\vec{k}+\overrightarrow{k_j}\right) e^{iP_{m,j}^{rec}\left(\vec{k}+\overrightarrow{k_j}\right)} - \beta A_{m,j}\left(\vec{k}+\overrightarrow{k_j}\right) e^{iP_{m,j}\left(\vec{k}+\overrightarrow{k_j}\right)}\right] \tag{5}$$

where α, β, and γ are coefficients that can be conveniently adjusted. In this work, we used the set of values $\alpha = 1$, $\beta = 1$, $\gamma = 1$ in simulations and $\alpha = 1$, $\beta = 0$, $\gamma = 1$ while processing experimental images. An iteration of the DSM algorithm occurs when the steps indicates in blocks (2)–(8) in Fig. 2 are successively done for each RP–FP image pair. Generally, several iterations are needed in order that the DSM algorithm convergence is established. Finally, as shown in block (9) in Fig. 2, a final Fourier transform operation provides the output high-resolution RP image and its corresponding phase. Fig. 3 shows DSM simulation results corresponding to an OD at the sample's plane with arbitrary intensity (Fig. 3(a)) and phase (Fig. 3(b)).

The simulation was conducted supposing that the sample was imaged with the experimental set up illustrated in Fig. 1 and illuminated successively from 44 different directions with the laser beam using

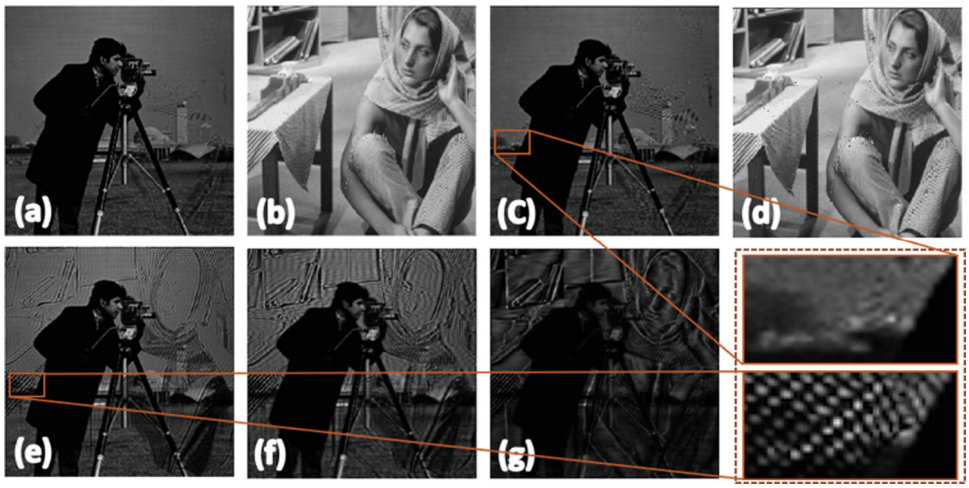

Fig. 3. Arbitrary (a) intensity and (b) phase of the simulated OD at the sample's plane. (c) High-resolution RP image and (d) corresponding phase obtained using the DSM algorithm. (e–g) Examples of simulated low-resolution RP image corresponding to different illumination directions.

all the circular holes of the HLG with $NA_c < NA_o$. No noise was added to the OD at the sample's plane. Fig. 3(c) and (d) show the intensity and recovered phase, respectively, corresponding to the high-resolution RP image obtained using the DSM algorithm sketched in Fig. 2. Convergence of the DSM algorithm was achieved after dozens of iterations. As expected, a very similar result was obtained using the FPM algorithm (not shown). Fig. 3(e)–(g) show examples of simulated low resolution RP images, which clearly contain traces of the phase of the OD at the sample's plane. In general, this is why the FPM algorithm permits to extract the phase from multiple low-resolution RP images. Different low-resolution RP images carry partial but different information about the phase of the electric field in the sample's plane. This variety is fundamental for the FPM phase-recovery algorithm success in extracting the unmeasured phase. A comparison of the insets in Fig. 3(c) and (e) shows that many details of the RP image are better defined in the high-resolution RP image than in the low-resolution RP images. This is in part because there are phase-artifacts present in the low-resolution RP images shown in Fig. 3(e)–(g) which are not present in the high-resolution RP image shown in Fig. 3(c). The simulation results shown in Fig. 3 confirm that DSM also permits to obtain a high-resolution RP image and recover the unmeasured phase of the optical disturbance for arbitrary samples. This was demonstrated before using less realistic one-dimensional simulations [19], but this is the first time that results of DSM full two-dimensional simulations are presented. In this work, the superposition in the FP space between consecutive FP images with small NA_o is ~86%, which is determined by the value of NA_o and the geometry of the used HDC and HLG. This value is larger than the minimum superposition values reported for FPM [21]; therefore, we expect that the experiments reported here could be optimized by reducing the number of images.

We also conducted simulations corresponding to the sample used in the experiments. We assumed an OD in the sample's plane which amplitude and phase are periodic with $p = 1.67$ μm, and we supposed that the sample was imaged with the experimental set up illustrated in Fig. 1 and illuminated successively from the same 44 different directions with the laser beam using the HLG. Fig. 4 shows simulation results obtained using the DSM algorithm.

Fig. 4(a) shows the synthetic FP image with large $NA_s = NA_o + NA_c = 1.53$ that was simulated using the DSM algorithm. We determine a distance of $\lambda/p \sim 0.33$ (in numerical aperture units, [14,15]) between the zero- and first-order diffraction spots in the synthetic FP image, which is in excellent correspondence with the period $p = 1.67$ determined from the simulated high-resolution RP image shown in Fig. 4(b). Moreover, the same periodicity is clearly visible in the recovered phase shown in Fig. 4(c).

4. Experimental results

We conducted experiments designed to study the influence of the size of the diffraction spots observed in the experimental FP images on the FOV of the high-resolution RP image that can be obtained using FPM and DSM. With this goal in mind, we imaged a commercial Ronchi Ruling with a relatively large period $p = 1.67$ μm using the experimental set up illustrated in Fig. 1. The sample was illuminated using the HDC in a first set of experiments and, in a second one, the laser-HLG combination was used. In both cases, a RP–FP image pair was obtained for each illumination direction with $NA_c < NA_o$. Dark field images ($NA_c > NA_o$) were not needed due to the relatively large period of the sample structure.

Fig. 5 shows several typical examples of the images that were experimentally obtained before implementing the phase-recovery algorithm. The images shown in Fig. 5(a)–(d) were obtained using the HDC while images shown in Fig. 5(e)–(h) were obtained using the laser-HLG

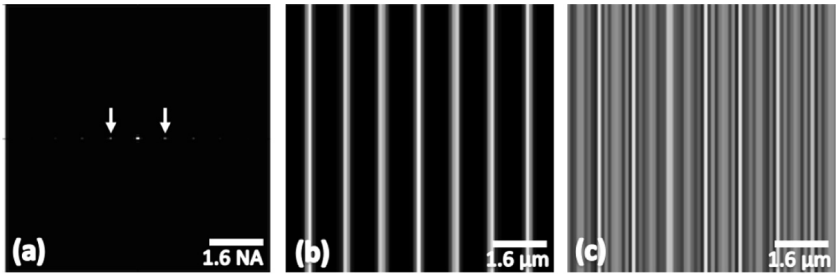

Fig. 4. Simulated (a) synthetic FP image and (b) high-resolution RP intensity image corresponding to a Ronchi Ruling with $p = 600$ lines/mm that were obtained using the DSM algorithm. (c) Recovered phase of the optical disturbance at the microscope's RP. The white arrows in (a) indicate the position of the first-order diffraction spots.

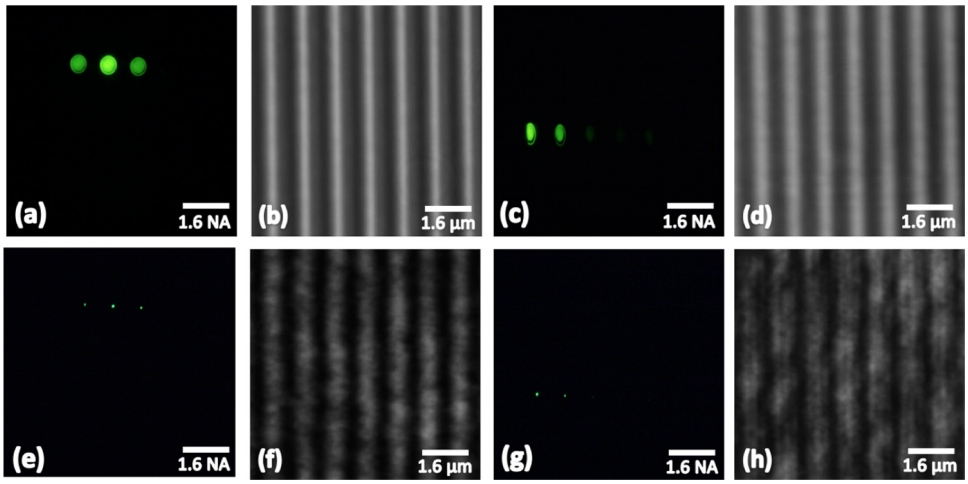

Fig. 5. Examples of experimental FP (a, c, e, g) and (b, d, f, h) RP images of a Ronchi Ruling target with $p = 1.67$ nm obtained using (a–d) the HDC and (e–f) the laser-HLG combination. The RP–FP image pairs were obtained for illumination directions corresponding to NA_c = (a–b, e–f) 0.58 and (c–d, g–h) 0.73.

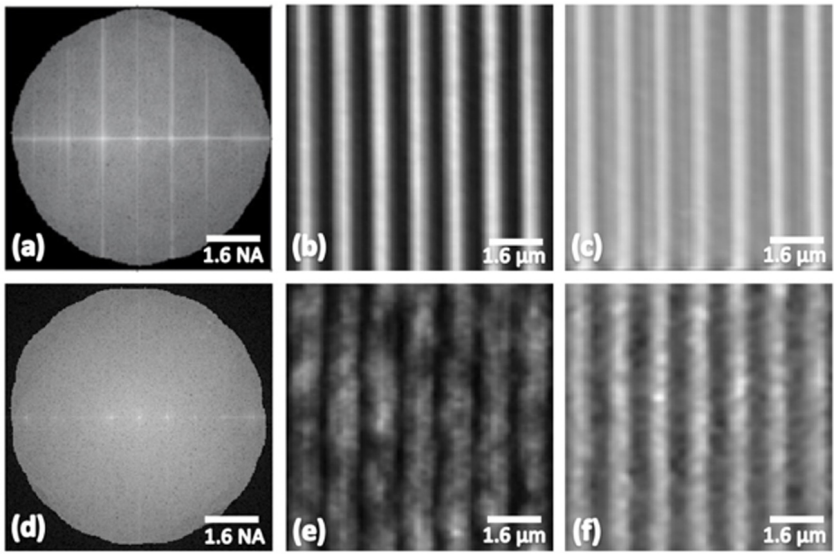

Fig. 6. Results obtained using the FPM algorithm when processing the experimental RP images obtained using (a–c) the HDC and (d–f) the laser-HLG combination. (a) And (d) synthetic FP images with $NA_s = 1.53$; (b) and (e) high-resolution RP images; (c) and (f) recovered phases.

combination. Three important characteristics can be identified after a comparison of these two set of images. First, as it should be expected, the experimental images obtained with LED illumination are very similar to the images obtained with the laser-HGL combination. Second, as it should also be expected, the RP images shown in Fig. 5(f) and (h) are noisier than the RP images shown in Fig. 5(b) and (d) due to the speckles associated to the higher coherence of the laser beam in comparison to the lower coherence of the light produced by a LED. And third, the diameter of the diffraction spots seen in the FP images shown in Fig. 5(a) and (c) are ~7 times larger than the diameter of the diffraction spots seen in the FP images shown in Fig. 5(e) and (g). This can be explained by the difference in the partial spatial and temporal coherence of both illumination sources [22–24]. Alternatively, the larger size of the diffraction spots produced by the LED illumination can be explained assuming each LED illuminates the sample with a cone of light formed by the incoherent superposition of plane waves impinging on the sample at slightly different directions [25]. The small divergence of the light emitted by LEDs should have little or no effect in the FPM technique because only RP images are used in FPM. This is confirmed by the FPM results shown in Fig. 6.

Fig. 6(a)–(c) (Fig. 6(d)–(f)) show results obtained by numerically processing the 44 experimental RP images obtained with the HDC (laser-HLG combination) using the FPM algorithm. As expected, the results are very similar in both cases except for the excess of noise present in Fig. 6(e) and (f), which is related with the use of noisier experimental images. Nevertheless, both high-resolution RP images shown in Fig. 6(b) and (e) have the correct period $p = 1.67$ µm of the Ronchi Ruling, which is in excellent correspondence to the separation $\lambda/p \sim 0.33$ between consecutive diffraction spots in the synthetic FP images with $NA_s = 1.53$ shown in Fig. 6(a) and (d). Moreover, as expected, the same periodicity is observed in the recovered phases shown in Fig. 6(c) and (f). In contrast to FPM, one should expect that the small divergence of the light emitted by LEDs should have a strong effect in the DSM technique because FP images are used in the DSM algorithm sketched in Fig. 2. This is confirmed by the DSM results shown in Fig. 7.

Fig. 7(a)–(c) (Fig. 7(d)–(f)) show results obtained by numerically processing the 44 experimental RP and FP images obtained with the HDC (laser-HLG combination) using the DSM algorithm. Diffraction spots corresponding to several diffraction orders are clearly visible in the synthetic FP images with $NA_s = 1.53$ shown in Fig. 7(a) and (d). However, as expected, the diameter of the diffraction spots in the

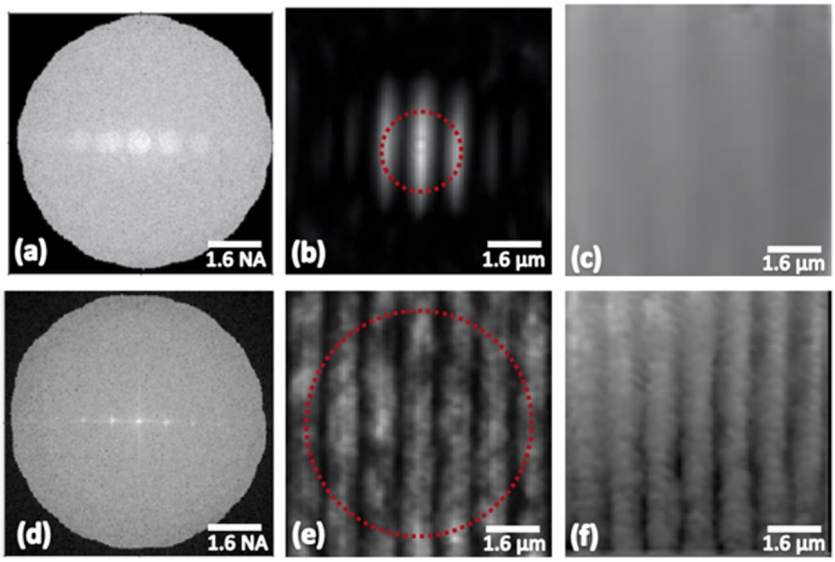

Fig. 7. Results obtained using the DSM algorithm when processing the experimental RP and FP images obtained using (a–c) the HDC and (d–f) the laser-HLG combination. (a) And (d) synthetic FP images with $NA_s = 1.53$; (b) and (e) high-resolution RP images; (c) and (f) recovered phases. The added discontinuous-line rings indicate the estimated FOV of the high-resolution RP images.

synthetic FP image shown in Fig. 7(a) is ~7 times larger than of the ones observed in the synthetic FP image shown in Fig. 7(d). There is a Fourier transform relationship between RP–FP images; therefore, larger diffraction spots in the FP image should produce reduced FOV in the RP image. In excellent correspondence with this observation the radius of the FOV of the high-resolution RP image shown in Fig. 7(e) is ~7 times larger than the really small FOV of the high-resolution RP image shown in Fig. 7(b). This is illustrated by the discontinuous-line rings added to Fig. 7(b) and (e), which radiuses were evaluated using the following equation [18]:

$$R \approx (\lambda/2\pi) * NA_{int} \tag{6}$$

where NA_{int} is the intrinsic numerical aperture associate to the divergence of the illumination beam, which we estimated from the experimental FP images to be $NA_{int} \sim 0.07$ for LEDs and $NA_{int} \sim 0.01$ for the laser beam. Nevertheless, in both high-resolution RP images shown in Fig. 7(b) and (e) the same periodicity $p = 1.67$ μm is clearly observed, which is in excellent correspondence to the separation $\lambda/p \sim 0.33$ between consecutive diffraction spots in the synthetic FP images shown in Fig. 7(a) and (d). A direct comparison of Fig. 7(c) and (f) shows that the phase was successfully recovered by the DSM algorithm when the laser-HLG combination was used (Fig. 7(f)) but failed to do so when using the HDC (Fig. 7(c)). A comparison of Fig. 7(f), Fig. 6(c), and (f) reveals a good correspondence between the phase recovered by laser-based DSM and the ones recovered using FPM. It should be noted that DSM requires double number of images than FPM and produces similar results than FPM for the sample used in this work; however, DSM should produce better results than FPM when imaging photonic crystals with a period smaller than the Rayleigh resolution limit [18]. In addition, the small FOV of the DSM-reconstructed RP image shown in Fig. 7(b) agree with previous reported results of DSM implemented using a HDC [18]. Therefore, the large FOV of the DSM-reconstructed RP image shown in Fig. 7(e) demonstrates that using a laser as the illumination source enhance the FOV due the decreasing in size of the diffraction spots in the corresponding experimental RP images.

5. Conclusions

We presented full two-dimensional DSM simulations for arbitrary samples, which demonstrate successful convergence of the DSM phase-recovery algorithm. We experimentally demonstrated that DSM implemented using a laser as the illumination source permits to obtain a synthetic OD with large FOV. However, the higher coherence of the light produced by a laser when compared with the light produced by LEDs results in additional noise affecting the quality of the obtained images. Therefore, we foresee two possible paths for transforming DSM in a useful super-resolution imaging technique. A first path consists in using a different source of illumination that combines the high intensity directionality of a laser with the low coherence of LEDs. For instance, the implementation of DSM using mode-locked lasers and random lasers should be explored. A second path consists in implementing a modified DSM algorithm that explicitly consider the partial spatial and temporal coherence of the illumination source.

Acknowledgments

This work was partially supported by the NSF Award (ECCS-1404394).

References

[1] D. Sayre, Some implications of a theorem due to Shannon, Acta Crystallogr. 5 (1952) 843.
[2] R.W. Gerchberg, W.O. Saxton, A practical algorithm for determination of phase from image and diffraction plane pictures, Optik 35 (1972) 237–245.
[3] J.R. Fienup, Reconstruction of an object from the modulus of its Fourier transform, Opt. Lett. 3 (1978) 27–29.
[4] J.R. Fienup, Phase retrieval algorithms: a comparison, Appl. Opt. 21 (1982) 2758–2769.
[5] H.M.L. Faulkner, J.M. Rodenburg, Movable aperture lensless transmission microscopy: A novel phase retrieval algorithm, Phys. Rev. Lett. 93 (2004) 023903.
[6] J.M. Rodenburg, A.C. Hurst, A.G. Cullis, B.R. Dobson, F. Pfeiffer, O. Bunk, C. David, K. Jefimovs, I. Johnson, Hard-X-ray lensless imaging of extended objects, Phys. Rev. Lett. 98 (2007) 034801.
[7] M. Humphry, B. Kraus, A. Hurst, A. Maiden, J. Rodenburg, Ptychographic electron microscopy using high-angle dark-field scattering for sub-nanometer resolution imaging, Nat. Commun 3 (2012) 730.
[8] A.M. Maiden, J.M. Rodenburg, M.J. Humphry, Optical ptychography: a practical implementation with useful resolution, Opt. Lett. 35 (2010) 2585–2587.
[9] A.M. Maiden, M.J. Humphry, F. Zhang, J.M. Rodenburg, Superresolution imaging via ptychography, J. Opt. Soc. Am. A 28 (2011) 604–612.
[10] G. Zheng, R. Horstmeyer, C. Yang, Wide-field, high-resolution Fourier ptychographic microscopy, Nat. Photonics 7 (2013) 739–745.
[11] L. Tian, X. Li, K. Ramchandran, L. Waller, Multiplexed coded illumination for Fourier ptychography with LED array microscope, Biomed. Opt. Express 14 (2014) 2376–2389.
[12] X. Ou, R. Horstmeyer, G. Zheng, C. Yang, High numerical aperture Fourier ptychography: principle, implementation and characterization, Opt. Express 23 (2015) 3472–3491.

[13] K. Guo, S. Dong, P. Nanda, G. Zheng, Optimization of sampling pattern and the design of Fourier ptychographic illuminator, Opt. Express 23 (2015) 6171–6180.
[14] S. Sen, D.B. Desai, M.H. Alsubaie, M.V. Zhelyeznyakov, L. Molina, H. Sari-Sarraf, A.A. Bernussi, L. Grave de Peralta, Imaging photonic crystals using Fourier plane imaging and Fourier ptychographic microscopy techniques implemented with a computer-controlled hemispherical digital condenser, Opt. Commun. 383 (2016) 500–507.
[15] S. Sen, A. Ishtiaque, B. Aljubran, A.A. Bernussi, L. Grave de Peralta, Fourier ptychographic microscopy using an infrared-emitting hemispherical digital condenser, Appl. Opt. 55 (2016) 6421–6427.
[16] C. Kuang, Y. Ma, R. Zhou, J. Lee, G. Barbasathis, R.R. Dasari, Z. Yaqoob, P.T. So, Digital micromirror device-based laser- illumination Fourier ptychographic microscopy, Opt. Express 23 (2015) 26999–27010.
[17] J. Chung, H. Lu, X. Ou, H. Zhou, C. Yang, Wide-field Fourier ptychographic microscopy using laser illumination source, Biomed. Opt. Express 7 (2016) 4787–4802.
[18] D.B. Desai, S. Sen, M.V. Zhelyeznyakov, W. Alenazy, L. Grave de Peralta, Super-resolution imaging of photonic crystals using dual-space microscopy, Appl. Opt. 55 (2016) 3929–3934.
[19] D.B. Desai, M.V. Zhelyeznyakov, S.A.S. Alanzi, L. Grave de Peralta, Simulation study of dual-space microscopy, Appl. Opt. 55 (2016) 7294–7300.
[20] J.W. Goodman, Introduction To Fourier Optics, third ed, McGraw-Hill, New York, 2005.
[21] S. Jiasong, Q. Chen, Y. Zhang, C. Zuo, Sampling criteria for Fourier ptychographic microscopy in object space and frequency space, Opt. Express 24 (2016) 15765–15781.
[22] J.W. Goodman, Statistical Optics, second ed, Wiley, New Jersey, 2015.
[23] J.N. Clark, X. Huang, R. Harder, I.K. Robinson, High-resolution three-dimensional partially coherent diffraction imaging, Nature Commun. 3 (2012) 993.
[24] R. Horstmeyer, C. Yang, A phase space model of Fourier ptychographic microscopy, Opt. Express 22 (2014) 338–358.
[25] R. Lopez-Boada, C.J. Regan, D. Dominguez, A.A. Bernussi, L. Grave de Peralta, Fundaments of optical far-field subwavelength resolution based on illumination with surface waves, Opt. Express 21 (2013) 11928–11942.